Conformal CVD-grown MoS2 on Three-dimensional Woodpile Photonic Crystals for Photonic Bandgap Engineering

Mike P. C. Taverne,[†,‡] Xu Zheng,[‡] Yu-Shao Jacky Chen,[‡] Katrina A. Morgan,[¶] Lifeng Chen,[‡] Nadira Meethale Palakkool,[†] Daniel Rezaie,[†] Habib Awachi,[†] John G. Rarity,[*,‡] Daniel W. Hewak,[¶] Chung-Che Huang,[*,¶] and Ying -Lung Daniel Ho[*,†,‡]

†*Department of Mathematics, Physics & Electrical Engineering, Northumbria University, NE1 8ST, Newcastle upon Tyne, UK*

‡*Department of Electrical and Electronic Engineering, University of Bristol, BS8 1UB, Bristol, UK*

¶*Optoelectronics Research Centre, University of Southampton, SO17 1BJ, Southampton, UK*

E-mail: john.rarity@bristol.ac.uk; cch@soton.ac.uk; daniel.ho@northumbria.ac.uk

Abstract

To achieve the modification of photonic band structures and realise the dispersion control towards functional photonic devices, composites of photonic crystal templates with high refractive index material are fabricated. A two-step process is used: 3D polymeric woodpile templates are fabricated by direct laser writing method followed by chemical vapour deposition of MoS_2. We observed red shifts of partial bandgaps at the near-infrared region when the thickness of deposited MoS_2 films increases. A

$\sim 10nm$ red shift of fundamental and high order bandgap is measured after each 1 nm MoS_2 thin film deposition and confirmed by simulations and optical measurements using angle-resolved Fourier imaging spectroscopy system.

Keywords

direct laser writing, two-photon lithography, chemical vapor deposition, chalcogenide materials, photonic bandgap, three-dimensional photonic crystals

1 Introduction

3D photonic crystals have a large range of applications due to their potential for showing omnidirectional photonic bandgaps.[1] This enables the creation of low-loss waveguides,[2,3] light bending,[2,4] waveguide splitters,[3] optical diodes,[5] negative refraction[6] and self-collimation[7] for example. Another possibility is the confinement of light in a small volume,[8–10] which has several applications in quantum technologies such as single-photon sources[11,12] and spin photon interfaces.[13]

Such 3D photonic crystals can be fabricated using Direct Laser Writing (DLW).[14] However this technique is limited to the fabrication of low refractive index polymeric materials, which leads to partial narrow bandgaps. Additional postprocessing, such as single[15,16] or double inverse backfilling[17] with high refractive index materials, is therefore usually necessary to obtain a full bandgap. Aside from full bandgaps, high refractive index contrast can also be used to tune photonic bands, open and enlarge bandgaps and control the dispersion of photonic crystals. This can be done using conformal coating with high refractive index materials. Such efforts have previously been made in one-dimensional (1D) photonic crystals[18] and butterfly wings (naturally occurring photonic crystals).[19] In 2005, Biswas et al. successfully demonstrated a full photonic bandgap at 6-7 µm by coating a polymeric three-dimensional (3D) woodpile structure[20,21] with titania (TiO_2).[22] Furthermore, in 2010,

Buso et al.[23] demonstrated bandgap shifts from a polymeric woodpile photonic crystal after coating it with successive 20nm CdS layers, with a shift of 375nm shift after an 80nm CdS coating.

Herein, a similar process is applied, but at a smaller scale (photonic bandgap at $\sim 1.3\mu m$) and using thin ($< 10\ nm$) molybdenum disulphide (MoS_2) films. MoS_2 has been gaining attention as an emerging material in various applications due to its properties such as semiconducting nature, high on/off current ratio (10^8) at room temperature and mobility of about 200 $cm^2(Vs)^{-1}$.[24–27] Bulk MoS_2 can act as an indirect bandgap semiconductor with high refractive index comparable to that of silicon, while monolayer MoS_2 possesses a direct band gap which makes it a good candidate for a light emitting medium. In this paper, we treat this material as bulk and focus on its high refractive index property. Conformally coated polymeric templates of photonic crystal structures could be used to enhance nonlinear optical responses of materials, such as MoS_2,[28] for highly efficient 3D all-optical switching for fast and energy-efficient memory devices.[29,30] MoS_2 is also an infrared transparent material and could therefore be a good candidate for mid-infrared sensing applications.[31,32]

For the polymeric templates, a woodpile structure[33] was chosen, as it is a well-known simple photonic crystal, that can be easily fabricated by using layer by layer lithographic approaches[34–36] (enabling mass production) or DLW.[37] Alternatively, Rod-Connected Diamond structures, which have larger bandgaps for identical index contrasts,[38] could be used instead in future work. However, these can only be made by DLW, so are limited to a slow writing process.

The fabrication procedure involves steps wherein 3D polymeric woodpile templates (see Figure 1) are fabricated by DLW, followed by low temperature chemical vapor deposition (CVD) of MoS_2 on it.[39] The optical properties of the composite structures are then examined by measuring reflection spectra changes after successive thin film coatings via our in-house built angle-resolved Fourier imaging spectroscopy (FIS) system.[15,40,41]

2 Geometry description

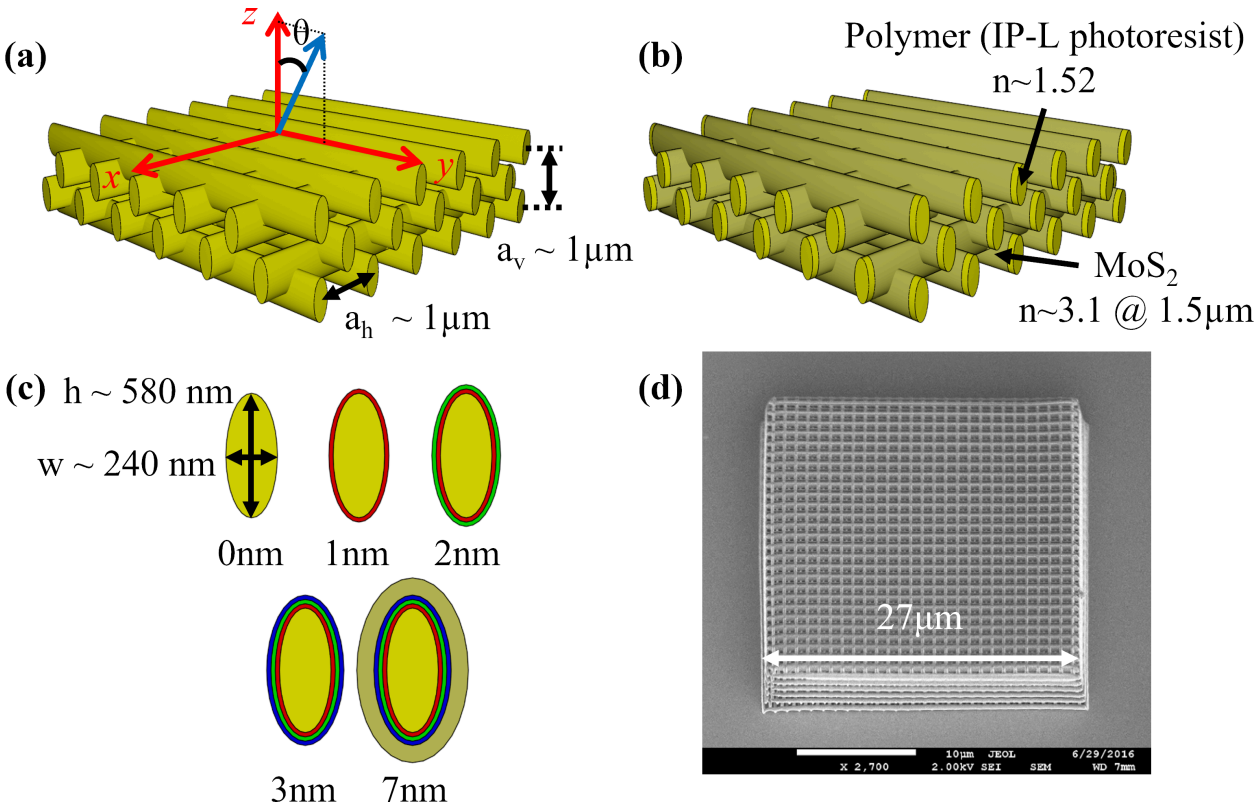

Figure 1: Simplified schematics of: (a) a non-coated woodpile template, (b) a thin film MoS_2-coated woodpile template, (c) the resulting rod cross sections after each MoS_2 thin film coating. Different colours are used to indicate the thin films coated in sequence. The scale of the thin film coatings relative to the inner polymer ellipse has been increased for clarity. (d) SEM image of the fabricated woodpile template.

Figures 1 (a)-(c) illustrate the design of the woodpile template and the thin film coatings and Figure 1 (d) shows a Scanning Electron Microscope (SEM) image of the fabricated woodpile template. The parameters of the fabricated Body-Centered Cubic (BCC) woodpile[42–44] are given as: $a_v = a_h = 1\mu m$, where a_v is the vertical period and a_h the lateral rod distance. The rod height $h \sim 580nm$ is larger than the rod width $w \sim 240nm$, due to the aspect ratio limitations in the write process.[45] The number of horizontal layers was $N_{layers} = 24$, while the number of rods in each layer alternated between $N_{rods} = 27$ and $N_{rods} = 28$, with the top two layers having 27 rods each. These parameters correspond to a BCC woodpile with $27 \times 27 \times 6$ periods. The size of the woodpile was $27 \times 27\mu m$.

3 Fabrication methods

The 3D polymeric woodpile templates (see Figure 1) were first fabricated by two-photon polymerization DLW (see Methods section), using a negative photoresist (IP-L 780, Nanoscribe GmbH). They were then subsequently coated with molybdenum disulphide (MoS_2) thin films using chemical vapour deposition (CVD), to achieve high refractive index contrast composites. The schematic diagram of the chemical vapour deposition setup used for MoS_2 thin film deposition in this project is shown in Figure 2 (modified from reference[39]).

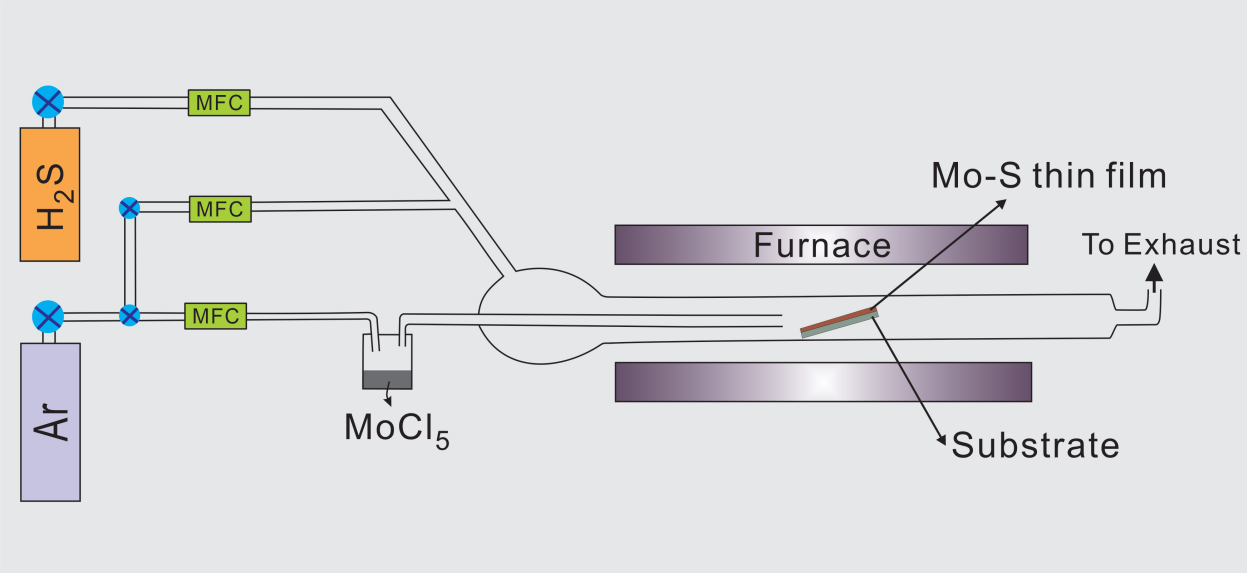

Figure 2: Schematic diagram of the chemical vapour deposition setup used for MoS_2 thin film deposition.

Firstly, a thin film of Mo-S is deposited on the woodpile templates' substrates using $MoCl_5$ as precursor, kept in a bubbler, delivered by Ar gas through a mass flow controller (MFC) to react with an H_2S/Ar gas mixture through another two MFCs at room temperature. The as-deposited Mo-S thin film could contain excess sulphur (S) and a small portion of unreacted Cl atoms. Hence, secondly, in order to convert the Mo-S-Cl composition to pure MoS_2, an annealing step in the H_2S atmosphere is needed. This annealing step is normally done at high temperature for several hours with the following gases: H_2S/Ar, 6% H_2/Ar.

This process can be described with the following chemical formula:

$$MoCl_5 + 2H_2S \rightarrow MoS_2 + 4HCl + {}^1/_2Cl_2$$

The deposition time, annealing temperature and the annealing time are the parameters affecting the thickness and the refractive index of the resulting MoS_2 thin film. Here, a thin film deposition for 30 minutes at room temperature and a following annealing treatment at 250° C for 3 hours is chosen to achieve a $\sim 1\ nm$ MoS_2 deposition, while avoiding any obvious thermal deformation of the woodpile templates. The first three layers of coatings were done for 30 minutes each, while the last coating was done for 120 minutes in order to observe a bigger shift, i.e. total deposition times of 30, 60, 90 and 210 minutes for the four coatings, leading to the following expected coating thicknesses: 1 nm, 2 nm, 3 nm and 7 nm.

The refractive index was measured using ellipsometry for a 10 nm thin film. For a wavelength of 1500 nm, the measured refractive index is $n \sim 3.1$ and the extinction coefficient $k \sim 0.62$ (Figure S1) and the absorption around 7% (Figure S2). Hence, for the simulations the refractive index for the MoS_2 coatings was taken as n=3.1. The material composition of the final MoS_2 layer coated on the surface of the woodpile was estimated using energy density x-ray spectroscopy (EDX) (Figure S3). The atomic percentage of sulphur and molybdenum was found to be in the ratio of approximately 2.5, confirming the presence of a mixture of MoS_2 (crystalline) and MoS_3 (amorphous).

The coating film thickness was estimated to be around 35 nm on the substrate by taking a Transmission Electron Microscopy (TEM) image of a cross-section slice and performing EDX mapping on it (Figure S4 and S5). However, the film thickness on the woodpile is expected to be less due to the increased surface area. Based on the woodpile parameters, the total surface area of the woodpile was calculated to be $A_{woodpile} \simeq 17333\ \mu m^2$, while the substrate area it sits on is $A_{substrate} = (27\ \mu m)^2 = 729\ \mu m^2$. This corresponds to a ratio $r = A_{woodpile}/A_{substrate} \simeq 24$. Assuming the deposited volume per substrate area is

the same and the coating is homogeneous, we would therefore expect a coating thickness of 35 $nm/r \simeq 1$ nm. Given the measurement results, the coating thickness on the woodpile is therefore likely to be between 1 nm and 35 nm.

4 Results and Discussion

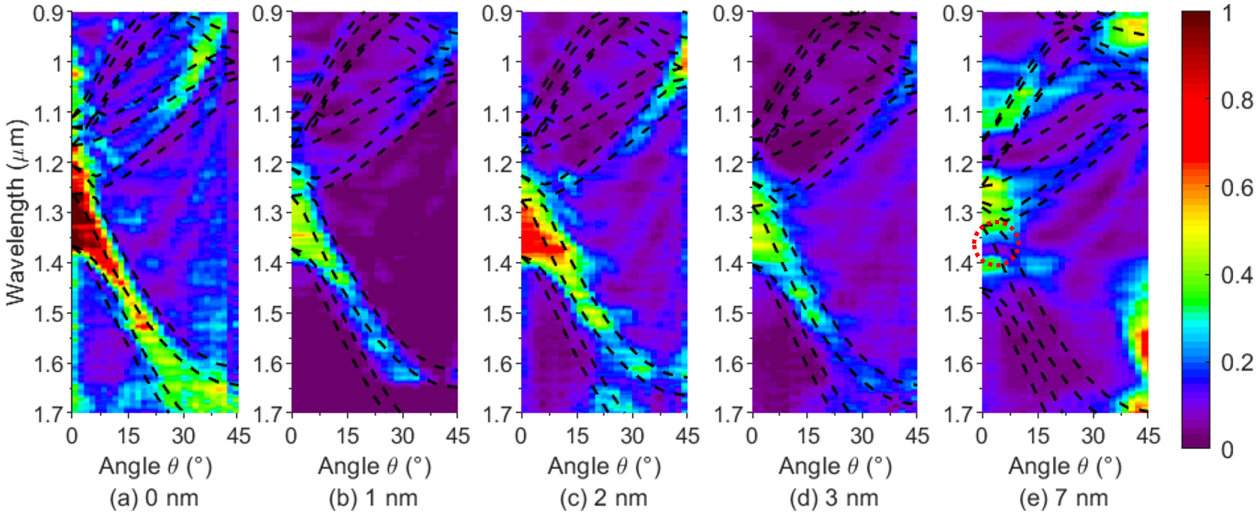

Figure 3: Measured angle-resolved reflection spectra of woodpile structures: (a) non-coated and (b) 1 nm, (c) 2 nm, (d) 3 nm, (e) 7 nm MoS_2 thin film coated. Dashed lines indicate their corresponding photonic band structures calculated via the PWE method. The red dashed circle in (e) highlights the splitting of the fundamental bandgap.

The resulting structures were analysed with an FIS system,[15] where reflection intensity is collected as a function of angle and wavelength (see Methods section), using white light illumination across the 0.9μm-1.7μm band. Figure 3 shows the results for S-polarized light (electric field along the X direction (Figure 1a)) measured as a function of the angle θ with increasing coating thicknesses from left to right. Dashed lines indicate their corresponding photonic band structures calculated via the Plane-Wave Expansion (PWE) method using the MIT Photonics Bands software,[46] with refractive index values of $n_{IP-L} = 1.52$ for the polymerized IP-L[41] and $n_{MoS_2} = 3.1$ for the MoS_2 coatings. As can be seen, both the fundamental and the high order gaps exhibited red shifts after each deposition.

Direct comparisons of the reflection spectra at normal incidence (for the fundamental

bandgap, between bands 2 and 3) and at 40° incidence (for the higher order bandgap, between bands 6 and 7) are shown in Figure 4. The vertical dashed and solid lines indicate the corresponding bandgap centres and edges calculated using PWE. We show the results at 40°, because this is the largest angle measurable with our existing setup. At 45°, there are technical limitations, due to being at the edge of the objective lens. As can be seen in Figure 3, there are strong reflection anomalies at large angles, especially in Figure 3e. These are due to glancing angle reflections, which are difficult to remove in our background correction methods.

As shown in Figure 3, each measurements exhibited two main bands: first, a band redshifting with increasing angle, corresponding to a grating like behaviour, and secondly a band blueshifting with increasing angle, corresponding to a behaviour similar to that of a Distributed Bragg Reflector (DBR). As the coating thickness increases both main bands redshift as result of the increasing effective refractive index. In the case of P-polarized incident light, the bandgaps are generally thinner, due to the weaker reflection of P-polarized light at non-normal incidence angles.[37] In addition, the grating-like redshifting band fades in favor of the DBR-like blueshifting band (See Figure S6).[42] Randomness in coating thickness is likely the cause of reduced band visibility in samples with the thickest coatings. At low thickness, it is clear that there is a good match between bands and measurements. Deviations will be due to fabrication errors and particularly the surface roughness, which increases with increasing coating thickness, thereby reducing the contrast between band and background. Furthermore, there is almost certainly a variation in coating thickness with depth into the sample, which effectively washes out the detail, particularly at high angle. The variability is evident, particularly at higher coating thickness.

From the sample with a 7 nm coating thickness, a splitting of the fundamental bandgap was observed (red dashed circle in Figure 3e). Moreover, it was not exhibiting the fundamental grating-like band. Rather than a shift in the bandgap, a change in the band structure was observed with a band at $\sim 1.4\mu m$ splitting off from the main bandgap moving towards

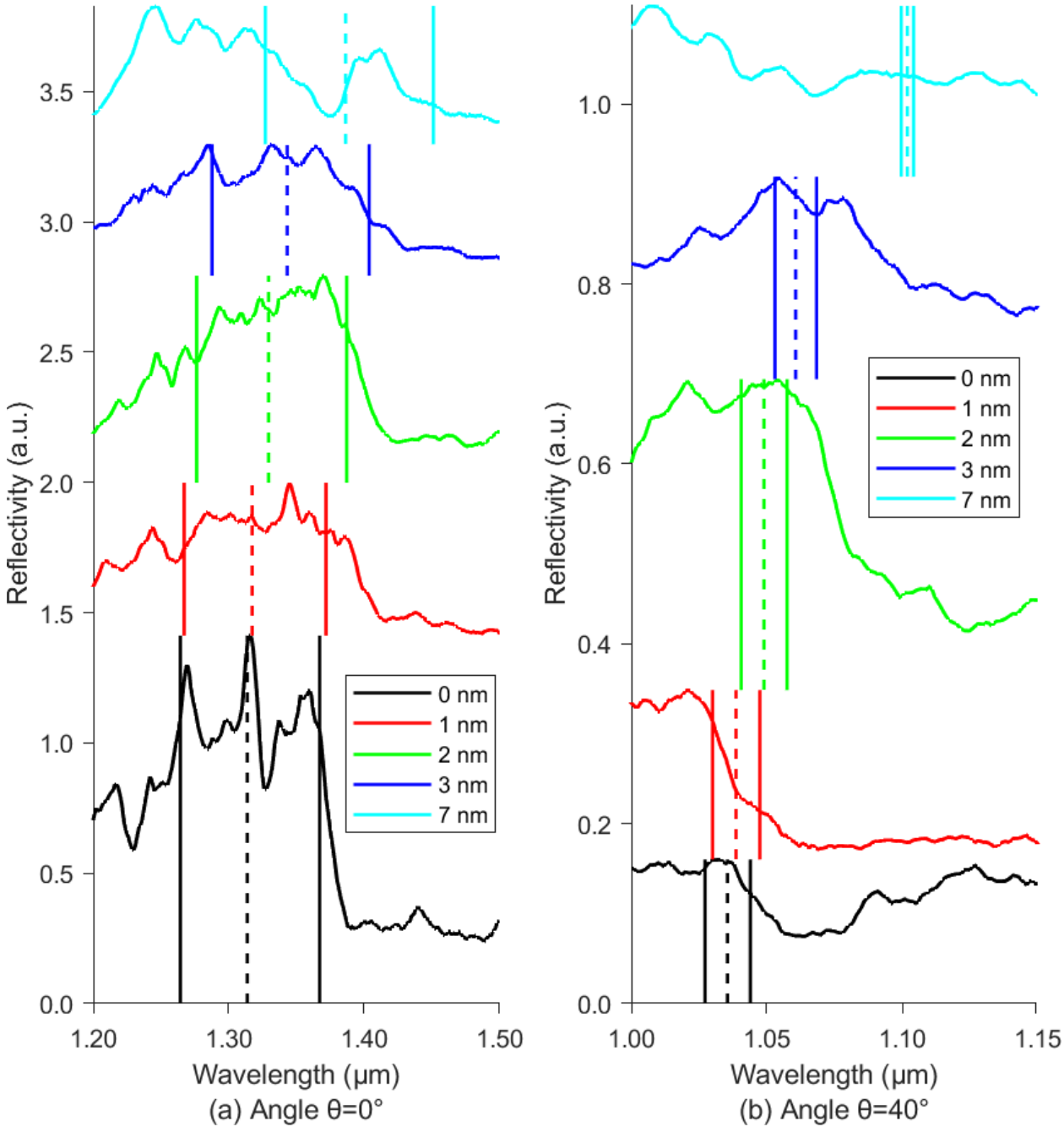

Figure 4: Measured reflection spectra from the woodpile template with varying MoS_2 thin film coating thicknesses: 0 nm (non-coated, solid-black), 1 nm (solid-red), 2 nm (solid-green), 3 nm (solid-blue) and 7 nm (solid-cyan) for angles of (a) 0° and (b) 40°. The vertical lines indicate the bandgap centres (dashed lines) and edges (solid lines) calculated using PWE of the gaps between bands 2 and 3 at 0° in (a) and between bands 6 and 7 at 40° in (b) for the corresponding coating thicknesses: 0 nm (non-coated, black), 1 nm (red), 2 nm (green), 3 nm (blue) and 7 nm (cyan).

the red. Although these trends are clearly visible in the 2D plots (Figure 3), it is a lot harder to discriminate the extent of redshift from single angle measurements due to the complex substructure of the band.

Figure 4a represents the measured reflection spectra corresponding to the reflection at 0°. When considering the long wavelength band edges (right vertical solid lines), a 5 nm redshift of the fundamental bandgap ($\sim 1.3\mu m$) was observed at normal incidence after the first 1 nm MoS_2 coating, followed by another two redshifts of 15 nm and 17 nm after the second and the third depositions respectively. At 0°, the long wavelength band edges of the measured reflection peaks match the calculated bandgap edges (right side). However as the thickness increases to 7 nm the splitting of the band puts the red-shifted peak close to the predicted red-shifted band. In the thinner coated structures it is difficult to see the substructure of the band making it difficult to confirm the small shifts predicted. In the reflection measurement corresponding to the 40° angle (Figure 4b), narrower peaks and distinct red shifts at the long wavelength band edges can be seen. However, it was difficult to accurately measure the exact band centres and edges. For the 1 nm coating (red curve), there is a first strongly visible band edge around 1.03µm, followed by a smaller drop around 1.05µm, corresponding to the expected band edge. At 7 nm coating thickness, the expected reflection peak is not visible. This is due to the corresponding bandgap being much narrower than the ones at thinner coatings, as well as a high angle anomalous scattering peak that suppresses it.

To predict the bandgap shifts for larger coating thicknesses, multiple PWE simulations were run and the midgap position and band edges of the fundamental bandgap (bands 2-3) at normal incidence and the higher order bandgap from band 6 to 7 at 40° incidence calculated for each simulation. Figure 5 shows the corresponding results. This confirms the observed redshifts with increasing coating thickness. The bandgap positions shift almost linearly with coating thickness, varying from 1.3 to 2.4 µm for the fundamental bandgap at normal incidence and from 1 to 2 µm for the higher order bandgap at 40° incidence as the coating increases from 0 to 130 nm.

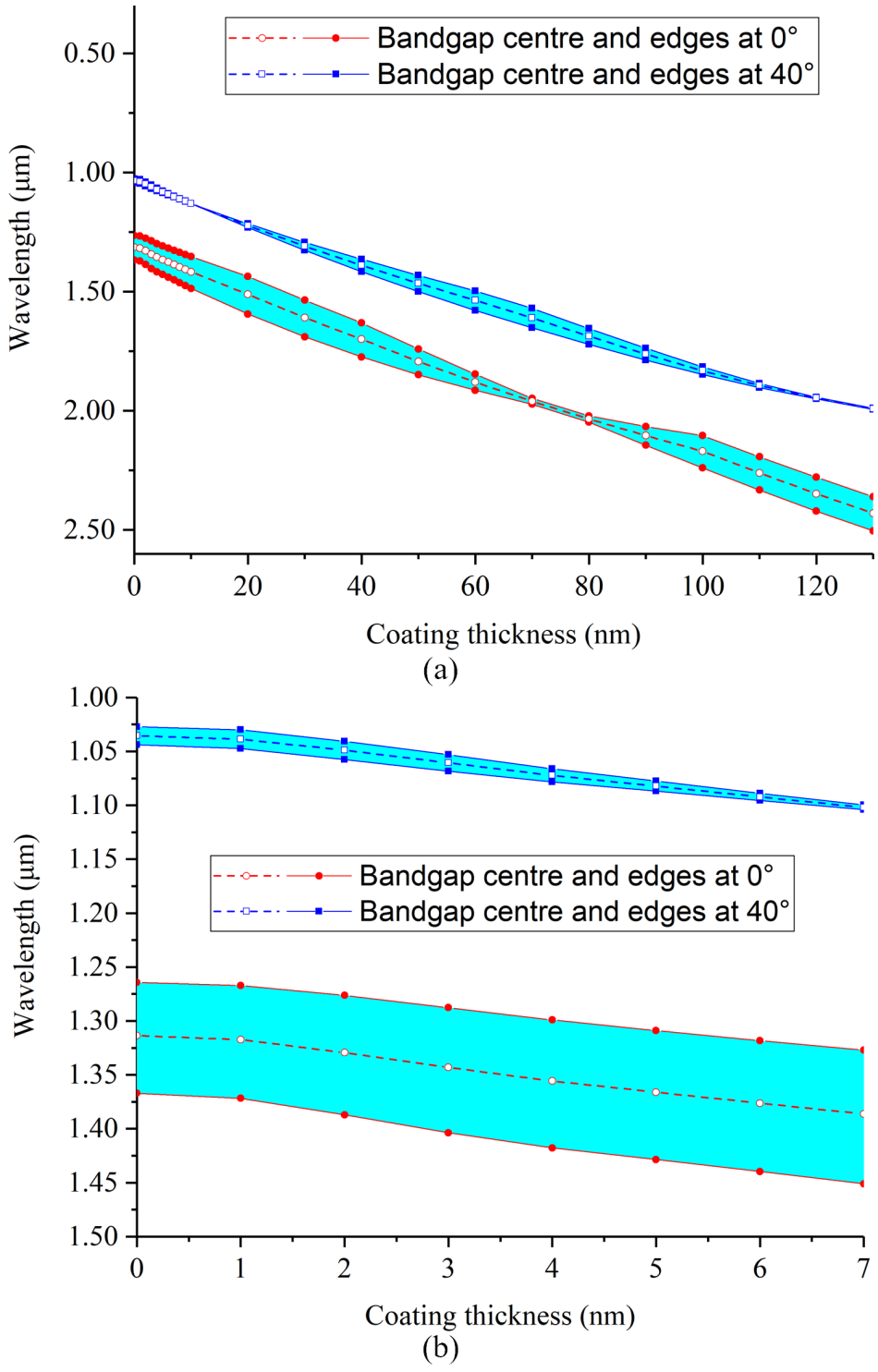

Figure 5: Calculated bandgap centres and edges vs coating thickness for the fundamental bandgap (bands 2-3) at normal incidence and the higher order bandgap from band 6 to 7 at incident angle 40° via the PWE method. The solid lines indicate the band edges, while the dashed lines indicate the corresponding centre (in terms of frequency). (a) Thickness from 0 to 130 nm, (b) from 0 to 7 nm.

5 Conclusion

Polymeric woodpile templates have been successfully fabricated and coated with multiple successive layers of MoS_2. Simulations of the structures show partial bandgaps in the short wave infra-red region with a 10 nm red shift occurring after each addition of 1 nm of MoS_2 thin film deposition. Measurement results are less easy to interpret. The 2D plots obtained from measuring scattering spectra as a function of angle (wave vector $\vec{k}$) show bandstructures with a small red shift observed with increasing thickness of the coating. By matching these results to the bandstructure simulations this becomes more apparent and helps calibrate the actual film thickness. However the substructure arising from the convergence of several bands makes it difficult to measure the redshifts in the zero degree spectral plot. As thickness of the coating increases the bands become less distinct which we ascribe to variations in coating thickness in the structure which smears the bandstructure. However, a clear redshifted band was observed in the thickest sample. In future work we aim to increase coating thickness to show clearer redshifts and strong wide angle bandgaps. The potential of our approach opens the way for developing a process to reliably engineer photonic bandgap materials through thin film deposition of MoS_2. Such conformally coated polymeric templates of photonic crystal structures could be used to enhance nonlinear optical responses for optical switching and sensing applications. Additionally, this work represents a step forward in determining the thicknesses of 3D wavelength scale structures with nanocoating thin-films by using an angle-resolved FIS system and expands the library of coating nanomaterials, leading to a wide range of future quantum and nanophotonic applications.

A Methods

A.1 Two-Photon Polymerization (2PP)

The Nanoscribe machine (*Nanoscribe Photonic Professional*) is a DLW system based on the 2PP method for the fabrication of arbitrary 3D nanostructures in photoresists such as IP-L.[47–49] The laser beam is produced by a femtosecond fibre laser (centre wavelength: 780 nm, average output power: 155mW, peak power: 25kW, pulse duration: 94fs, repetition rate: 80MHz) and focused into the photoresist through an oil-immersion objective lens with a NA of 1.4 and 100× magnification. The photoresist is drop-cast onto a substrate glass, which is glued on the piezoelectric 3D scanning stage.

A.2 Fourier Imaging Spectroscopy (FIS)

An identical system as that of our previous work[15,40] has been used here. This home-built Fourier imaging spectroscope uses a 4x objective lens to collimate a fiber (200 µm diameter) coupled white light source (Bentham Ltd. WLS100 300-2500 nm), focusing the light beam with an NA = 0.9, 60x objective lens on the sample. The detection plane is a projection image for the backfocal plane of the objective lens. This image is scanned by a fiber (105 µm diameter) attaches to a x-y motorized stage, the other end of the fiber connects to a spectrometer (Ocean optics NIRQuest512), which has 900-1700 nm spectrum range. The angular resolution of the system is $\sim 2^{\circ}$ per scan step.

Acknowledgments

This work was carried out using the computational facilities of the Advanced Computing Research Centre, University of Bristol, Bristol, UK and was funded by the Engineering and Physical Sciences Research Council (EPSRC) grants EP/M009033/1, EP/M024458/1, EP/V040030/1, EP/M008487/1 and EP/N00762X/1, and the Royal Society research grant

RGS\R1\221031.

Supporting Information Available

The Supporting Information is available free of charge at [supporting_information.pdf].

- supporting_information.pdf: Additional information about the optical properties of MoS_2; EDX and TEM analysis of the thin film coating; Reflection spectra for S and P-polarized incident light.

References

(1) Butt, M.; Khonina, S.; Kazanskiy, N. Recent advances in photonic crystal optical devices: A review. *Optics & Laser Technology* **2021**, *142*, 107265.

(2) Lin, S. Experimental Demonstration of Guiding and Bending of Electromagnetic Waves in a Photonic Crystal. *Science* **1998**, *282*, 274–276.

(3) Fan, S.; Johnson, S. G.; Joannopoulos, J. D.; Manolatou, C.; a. Haus, H. Waveguide branches in photonic crystals. *Journal of the Optical Society of America B* **2001**, *18*, 162.

(4) Zhang, Y.; Li, B. Photonic crystal-based bending waveguides for optical interconnections. *Optics Express* **2006**, *14*, 5723–5732.

(5) Liu, B.; Liu, Y.-F.; Jia, C.; He, X.-D. All-optical diode structure based on asymmetrical coupling by a micro-cavity and FP cavity at two sides of photonic crystal waveguide. *AIP Advances* **2016**, *6*, 065316.

(6) Notomi, M. Negative refraction in photonic crystals. *Optical and quantum electronics* **2002**, *34*, 133–143.

(7) Noori, M.; Soroosh, M.; Baghban, H. Self-collimation in photonic crystals: applications and opportunities. *Annalen der Physik* **2018**, *530*, 1700049.

(8) Taverne, M. P. C.; Ho, Y.-L. D.; Zheng, X.; Chen, L.; Fang, C.-H. N.; Rarity, J. Strong light confinement in rod-connected diamond photonic crystals. *Opt. Lett.* **2018**, *43*, 5202–5205.

(9) Taverne, M. P. C.; Ho, Y.-L. D.; Zheng, X.; Liu, S.; Chen, L.-F.; Lopez-Garcia, M.; Rarity, J. G. Modelling defect cavities formed in inverse three-dimensional rod-connected diamond photonic crystals. *EPL (Europhysics Letters)* **2016**, *116*, 64007.

(10) John, S. Strong localization of photons in certain disordered dielectric superlattices. *Phys. Rev. Lett.* **1987**, *58*, 2486–2489.

(11) Moczała-Dusanowska, M.; Łukasz Dusanowski,; Gerhardt, S.; He, Y. M.; Reindl, M.; Rastelli, A.; Trotta, R.; Gregersen, N.; Höfling, S.; Schneider, C. Strain-Tunable Single-Photon Source Based on a Quantum Dot–Micropillar System. *ACS Photonics* **2019**, *6*, 2025–2031, doi: 10.1021/acsphotonics.9b00481.

(12) Aharonovich, I.; Englund, D.; Toth, M. Solid-state single-photon emitters. *Nature Photonics* **2016**, *10*, 631–641.

(13) Lodahl, P.; Mahmoodian, S.; Stobbe, S.; Rauschenbeutel, A.; Schneeweiss, P.; Volz, J.; Pichler, H.; Zoller, P. Chiral quantum optics. *Nature* **2017**, *541*, 473–480.

(14) Hunt, M.; Taverne, M.; Askey, J.; May, A.; Van Den Berg, A.; Ho, Y.-L. D.; Rarity, J.; Ladak, S. Harnessing Multi-Photon Absorption to Produce Three-Dimensional Magnetic Structures at the Nanoscale. *Materials* **2020**, *13*.

(15) Chen, L.; Morgan, K. A.; Alzaidy, G. A.; Huang, C.-C.; Ho, Y.-L. D.; Taverne, M. P. C.; Zheng, X.; Ren, Z.; Feng, Z.; Zeimpekis, I.; Hewak, D. W.; Rarity, J. G. Observation of

Complete Photonic Bandgap in Low Refractive Index Contrast Inverse Rod-Connected Diamond Structured Chalcogenides. *ACS Photonics* **2019**, *6*, 1248–1254.

(16) Tétreault, N.; von Freymann, G.; Deubel, M.; Hermatschweiler, M.; Pérez-Willard, F.; John, S.; Wegener, M.; Ozin, G. A. New Route to Three-Dimensional Photonic Bandgap Materials: Silicon Double Inversion of Polymer Templates. *Advanced Materials* **2006**, *18*, 457–460.

(17) Hermatschweiler, M.; Ledermann, A.; Ozin, G. A.; Wegener, M.; von Freymann, G. Fabrication of Silicon Inverse Woodpile Photonic Crystals. *Advanced Functional Materials* **2007**, *17*, 2273–2277.

(18) Tolmachev, V. A.; Perova, T. S.; Berwick, K. Design of one-dimensional composite photonic crystals with an extended photonic band gap. *Journal of Applied Physics* **2006**, *99*, 033507.

(19) Gaillot, D. P.; Deparis, O.; Welch, V.; Wagner, B. K.; Vigneron, J. P.; Summers, C. J. Composite organic-inorganic butterfly scales: Production of photonic structures with atomic layer deposition. *Phys. Rev. E* **2008**, *78*, 031922.

(20) Zheng, X.; Taverne, M. P. C.; Ho, Y.-L. D.; Rarity, J. G. Cavity Design in Woodpile Based 3D Photonic Crystals. *Applied Sciences* **2018**, *8*.

(21) Taverne, M. P. C.; Ho, Y.-L. D.; Rarity, J. G. Investigation of defect cavities formed in three-dimensional woodpile photonic crystals. *J. Opt. Soc. Am. B* **2015**, *32*, 639–648.

(22) Biswas, R.; Ahn, J.; Lee, T.; Lee, J.-H.; Kim, Y.-S.; Kim, C.-H.; Leung, W.; Oh, C.-H.; Constant, K.; Ho, K.-M. Photonic bandgaps of conformally coated structures. *J. Opt. Soc. Am. B* **2005**, *22*, 2728–2733.

(23) Buso, D.; Nicoletti, E.; Li, J.; Gu, M. Engineering the refractive index of three-

dimensional photonic crystals through multilayer deposition of CdS films. *Opt. Express* **2010**, *18*, 1033–1040.

(24) Wadhwa, R.; Agrawal, A. V.; Kumar, M. A strategic review of recent progress, prospects and challenges of MoS_2-based photodetectors. *Journal of Physics D: Applied Physics* **2021**, *55*, 063002.

(25) Samy, O.; El Moutaouakil, A. A Review on MoS2 Energy Applications: Recent Developments and Challenges. *Energies* **2021**, *14*.

(26) Gupta, D.; Chauhan, V.; Kumar, R. A comprehensive review on synthesis and applications of molybdenum disulfide (MoS2) material: Past and recent developments. *Inorganic Chemistry Communications* **2020**, *121*, 108200.

(27) Mak, K. F.; Lee, C.; Hone, J.; Shan, J.; Heinz, T. F. Atomically Thin MoS_2: A New Direct-Gap Semiconductor. *Phys. Rev. Lett.* **2010**, *105*, 136805.

(28) Woodward, R. I.; Murray, R. T.; Phelan, C. F.; de Oliveira, R. E. P.; Runcorn, T. H.; Kelleher, E. J. R.; Li, S.; de Oliveira, E. C.; Fechine, G. J. M.; Eda, G.; de Matos, C. J. S. Characterization of the second- and third-order nonlinear optical susceptibilities of monolayer MoS2 using multiphoton microscopy. *2D Materials* **2016**, *4*, 011006.

(29) Ngo, Q. M.; Kim, S.; Lee, J.; Lim, H. All-Optical Switches Based on Multiple Cascaded Resonators With Reduced Switching Intensity-Response Time Products. *Journal of Lightwave Technology* **2012**, *30*, 3525–3531.

(30) Ngo, Q. M.; Le, K. Q.; Lam, V. D. Optical bistability based on guided-mode resonances in photonic crystal slabs. *J. Opt. Soc. Am. B* **2012**, *29*, 1291–1295.

(31) Kumar, S.; Meng, G.; Mishra, P.; Tripathi, N.; Bannov, A. G. A systematic review on 2D MoS2 for nitrogen dioxide (NO2) sensing at room temperature. *Materials Today Communications* **2023**, *34*, 105045.

(32) Lambrecht, A.; Schmitt, K. In *Mid-infrared Optoelectronics*; Tournié, E., Cerutti, L., Eds.; Woodhead Publishing Series in Electronic and Optical Materials; Woodhead Publishing, 2020; pp 661–715.

(33) Ho, K.-M. K.; Chan, C.; Soukoulis, C.; Biswas, R.; Sigalas, M. Photonic band gaps in three dimensions: New layer-by-layer periodic structures. *Solid State Communications* **1994**, *89*, 413–416.

(34) Aoki, K. Practical approach for a rod-connected diamond photonic crystal operating at optical wavelengths. *Applied Physics Letters* **2009**, *95*, 191910.

(35) Aoki, K.; Miyazaki, H. T.; Hirayama, H.; Inoshita, K.; Baba, T.; Sakoda, K.; Shinya, N.; Aoyagi, Y. Microassembly of semiconductor three-dimensional photonic crystals. *Nature Materials* **2003**, *2*, 117–121.

(36) Qi, M.; Lidorikis, E.; Rakich, P. T.; Johnson, S. G.; Joannopoulos, J. D.; Ippen, E. P.; Smith, H. I. A three-dimensional optical photonic crystal with designed point defects. *Nature* **2004**, *429*, 538–542.

(37) Deubel, M.; Wegener, M.; Linden, S.; von Freymann, G. Angle-resolved transmission spectroscopy of three-dimensional photonic crystals fabricated by direct laser writing. *Applied Physics Letters* **2005**, *87*, 221104.

(38) Men, H.; Lee, K. Y. K.; Freund, R. M.; Peraire, J.; Johnson, S. G. Robust topology optimization of three-dimensional photonic-crystal band-gap structures. *Optics Express* **2014**, *22*, 22632.

(39) Huang, C.-C.; Al-Saab, F.; Wang, Y.; Ou, J.-Y.; Walker, J. C.; Wang, S.; Gholipour, B.; Simpson, R. E.; Hewak, D. W. Scalable high-mobility MoS2 thin films fabricated by an atmospheric pressure chemical vapor deposition process at ambient temperature. *Nanoscale* **2014**, *6*, 12792–12797.

(40) Chen, L.; Lopez-Garcia, M.; Taverne, M. P. C.; Zheng, X.; Ho, Y.-L. D.; Rarity, J. Direct wide-angle measurement of a photonic band structure in a three-dimensional photonic crystal using infrared Fourier imaging spectroscopy. *Opt. Lett.* **2017**, *42*, 1584–1587.

(41) Chen, L.; Taverne, M. P. C.; Zheng, X.; Lin, J.-D.; Oulton, R.; Lopez-Garcia, M.; Ho, Y.-L. D.; Rarity, J. G. Evidence of near-infrared partial photonic bandgap in polymeric rod-connected diamond structures. *Opt. Express* **2015**, *23*, 26565–26575.

(42) Zheng, X. Simulation and Fabrication of Woodpile-Based Photonic Crystal Structures and Their Applications. Ph.D. thesis, 2017.

(43) Taverne, M. Modelling and fabrication of nanophotonics devices. Ph.D. thesis, 2017; https://research-information.bris.ac.uk/en/studentTheses/modelling-and-fabrication-of-nanophotonics-devices.

(44) Staude, I.; Thiel, M.; Essig, S.; Wolff, C.; Busch, K.; von Freymann, G.; Wegener, M. Fabrication and characterization of silicon woodpile photonic crystals with a complete bandgap at telecom wavelengths. *Optics letters* **2010**, *35*, 1094–6.

(45) Fischer, J.; Wegener, M. Three-dimensional optical laser lithography beyond the diffraction limit. *Laser & Photonics Reviews* **2013**, *7*, 22–44.

(46) Johnson, S.; Joannopoulos, J. Block-iterative frequency-domain methods for Maxwell's equations in a planewave basis. *Optics express* **2001**, *8*, 173–190.

(47) Hahn, V.; Kiefer, P.; Frenzel, T.; Qu, J.; Blasco, E.; Barner-Kowollik, C.; Wegener, M. Rapid Assembly of Small Materials Building Blocks (Voxels) into Large Functional 3D Metamaterials. *Advanced Functional Materials* **2020**, *30*, 1907795.

(48) Saha, S. K.; Divin, C.; Cuadra, J. A.; Panas, R. M. Effect of Proximity of Features

on the Damage Threshold During Submicron Additive Manufacturing Via Two-Photon Polymerization. *Journal of Micro and Nano-Manufacturing* **2017**, *5*, 031002.

(49) Jiang, L. J.; Campbell, J. H.; Lu, Y. F.; Bernat, T.; Petta, N. Direct Writing Target Structures by Two-Photon Polymerization. *Fusion Science and Technology* **2016**, *70*, 295–309.

TOC Graphic